CHEMISTRY OF MATERIALS

ARTICLE

pubs.acs.org/cm

Selective Surfaces: High-Surface-Area Zinc Tin Sulfide Chalcogels

Youngtak Oh, Santanu Bag, Christos D. Malliakas, and Mercouri G. Kanatzidis*

Department of Chemistry, Northwestern University, 2145 Sheridan Rd., Evanston, Illinois 60208, United States

Supporting Information

ABSTRACT: Porous zinc tin sulfide aerogel materials were constructed by metathesis reactions between $Zn(acac)_2 \cdot H_2O$ and tetrahedral thiostannate cluster salts containing discrete $[SnS_4]^{4-}$, $[Sn_2S_6]^{4-}$, and $[Sn_4S_{10}]^{4+}$ units. Self-assembly reactions of the Zn^{2+} linker and anionic thiostannate clusters yielded polymeric random Zn/Sn/S networks with gelation properties. Supercritical drying of the gels and solvent/counterion removal resulted in a metal sulfur framework. $Zn_2Sn_xS_{2x+2}$ (x = 1, 2, 4) aerogels showed high surface areas (363−520 m^2/g) and pore volumes (1.1−1.5 cm^3/g), and wide bandgap energies (2.8−3.2 eV). Scanning and transmission electron microscopy studies show the pores are micro- (d < 2 nm), meso- (2 nm < d < 50 nm), and macro- (d > 50 nm) regions. The zinc chalcogenide aerogels also possess high affinities toward soft heavy metals and reversible absorption of strong electron-accepting molecules.

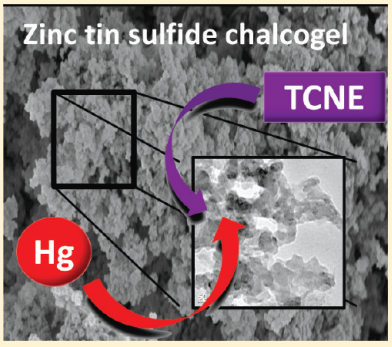

KEYWORDS: porous materials, gas absorption, gas separation, chalcogenides, heavy metal removal

INTRODUCTION

Aerogels are a unique class of porous materials that are largely composed of randomly interconnected nanoparticles. Aerogels possess low density and high internal surface area, which lead to potential applications such as catalysis,[1−5] separations,[6] sensing devices,[7,8] and charge storage.[9] The majority of aerogel studies are based on oxide materials, such as SiO_2, Al_2O_3, and TiO_2 or carbon-based materials.[10] However, nonoxide counterparts also merit strong interest, because of the unique combination of accessible open frameworks, high surface areas, surfaces with soft Lewis basicities, and more-attractive electronic properties that are relevant for photocatalysis,[11] photoconductivity,[12] photovoltaic cells,[13,14] electroluminescence,[15−18] and water remediation.[19,20] The field of nonoxide aerogels is relatively unexplored, and only limited studies have been reported. This may be partially because of the difficulties in preparing and handling precursors, the complexities of synthesis, and the ability to obtain gels.[15,17,21−26]

Chalcogenide cluster-based aerogels, nicknamed chalcogels, are a new class of porous materials and have been made using a simple metathesis reaction between cationic transition-metal linkers and anionic chalcogenide clusters.[19,20,27,28] This strategy offers a direct synthetic method for obtaining monolithic porous semiconducting aerogels with advantages in device adaptation and reproduction. The platinum-based chalcogel system, $Pt[M_xQ_{2x+2}]$ (where M = Ge, Sn; Q = S, Se, Te; and x = 1, 2, 4), uses germanium or tin chalcogenide clusters as anionic building blocks and platinum ions as a linking metals.[20] The platinum-based chalcogels display tunable electron bandgap energies, depending on the choice of cluster units. The synthesis of chalcogels derived from Sb^{3+} and Sn^{2+} linkers and $[Sn_2S_6]^{4-}$ and $[SnS_4]^{4-}$ building blocks has also been reported with the mixed-metal $Pt/Sb/Ge_4Se_{10}$ chalcogel exhibiting high gas selectivity toward CO_2/C_2H_6 over H_2.[29]

For the metathesis reaction to succeed in providing a gel, the inorganic species should engage in a slow self-assembly process. In many cases, many of the transition-metal linkers react too rapidly with chalcogenide clusters to form precipitates without gelation or do not form extended networks and therefore remain in solution without further polymerization and gelation. In order to obtain a porous metal-chalcogenide system that undergoes gelation, proper metal precursors are important to control the polymerization rate of the inorganic framework. In this work, we have extended the metathesis route of constructing metal-chalcogenide aerogels of Zn^{2+}-coordinated thiostannate aerogels with $[SnS_4]^{4-}$, $[Sn_2S_6]^{4-}$, $[Sn_4S_{10}]^{4-}$ clusters in formamide solution. The resulting zinc tin sulfide aerogels possess high surface areas and large pore volumes. Their sulfidic surfaces provide high selectivity toward soft heavy-metal ions, such as Hg^{2+}, and high efficiency of removing those metal ions from aqueous media. We also show, for the first time, that the Zn−Sn−S chalcogel is a capable of reversible absorption of electron-accepting molecules. The latter process involves organic molecules such as tetracyanoethylene (TCNE) via a charge-transfer process, which gives rise to an active shift of the optical band gap. Therefore, these chalcogels can discriminate among organic molecules, based on their electronic structure.

EXPERIMENTAL SECTION

Synthesis of Starting Materials. *$Na_4SnS_4 \cdot 14H_2O$.* $Na_4SnS_4 \cdot 14H_2O$ was used as a precursor to provide $[SnS_4]^{4-}$ anions when dissolved. An amount of 28.89 g (120 mmol) of $Na_2S \cdot 9H_2O$ (Aldrich, 99%) was dissolved in 100 mL of H_2O with stirring. Then, 7.8 g

Received: February 2, 2011
Revised: March 10, 2011
Published: April 05, 2011

(30 mmol) of $SnCl_4 \cdot 5H_2O$ (Aldrich, 98%) was dissolved in H_2O and added dropwise to the $Na_2S \cdot 9H_2O$ solution with continuous stirring. The solution was kept at 45 °C for 8 h and then added to 400 mL of methanol and stored in a refrigerator for 48 h. Precipitated white crystals of $Na_4SnS_4 \cdot 14H_2O$ were washed with EtOH and dried under vacuum for 24 h. The final product yield was 73%, based on $SnCl_4 \cdot 5H_2O$.

$Na_4Sn_2S_6 \cdot 14H_2O$. $Na_4Sn_2S_6 \cdot 14H_2O$ was used as a source of $[Sn_2S_6]^{4-}$ chalcogenide clusters during the metathesis reaction. To synthesize $Na_4Sn_2S_6 \cdot 14H_2O$, a similar method was adopted. A 3:1 ratio of $Na_2S \cdot 9H_2O$ (14.4 g; 60 mmol) and $SnCl_4 \cdot 5H_2O$ (5.2 g; 20 mmol) was reacted in 100 mL of H_2O for 8 h and the resulting solution was added to 300 mL of acetone. With vigorous stirring, a light yellow emulsion was formed in solution and resulted in a white precipitate. The solution was kept in a refrigerator for 48 h and the resulting white crystals of $Na_4Sn_2S_6 \cdot 14H_2O$ of were filtered, washed with acetone, and dried in a vacuum oven for 24 h yielding 65% of total product.

$[(CH_3CH_2)_4N]_4Sn_4S_{10}$. $[(CH_3CH_2)_4N]_4Sn_4S_{10}$ was used as a source of $[Sn_4S_{10}]^{4-}$, which is an adamantane tetrahedral cluster. In an evacuated fused silica tube, 220 mg (2 mmol) of K_2S, 474 mg (4 mmol) of Sn, and 256 mg (8 mmol) of S were reacted by a direct flame (500−600 °C) to yield a product with a stoichiometric composition of $K_2Sn_2S_5$.[30] The resulting $K_2Sn_2S_5$ (1 mmol) was reacted with $(CH_3CH_2)_4NBr$ (4 mmol) in ethylenediamine at 100 °C under N_2, filtered, and washed with 50 mL of ethanol. The light gray powder of $[(CH_3CH_2)_4N]_4Sn_4S_{10}$ obtained was dried in the vacuum oven for 24 h and 54% yield was produced.

Synthesis of Zinc Tin Sulfur (ZTS) Wet Gel. An amount of 2 mmol (520 mg) of Zn(acetylacetonate)$\cdot H_2O$ (Sigma−Aldrich, 99.995%) was dissolved in 10 mL of formamide and 1 mmol of the corresponding tin sulfide precursor ($Na_4SnS_4 \cdot 14H_2O$, ∼590 mg; $Na_4Sn_2S_6 \cdot 14H_2O$, ∼770 mg; $[(CH_3CH_2)_4N]_4Sn_4S_{10}$, ∼925 mg) was added to 10 mL of formamide in a separate vial. The zinc precursor solution was added slowly into the tin sulfide precursor solution with stirring, yielding a cloudy suspension. Slight heating and vigorous stirring were required to obtain a clear solution. When the precursor salts were completely dissolved, the solution was transferred to a clean glass vial and placed in a sand bath (60 °C) for 5−10 d. As the polymerization occurred, the viscosity of the solution increased, which eventually solidified to a monolithic gel. The remaining formamide was decanted and the gel was soaked in an $EtOH/H_2O$ (4:1) solution for 3 d and then in 100% EtOH for 7 d, to remove byproducts and impurities. A fresh supply of soaking solvent ($EtOH/H_2O$ and EtOH) was provided every 24 h.[31]

Supercritical Drying of Wet Gels. A Tousimis Autosamdri-815B Series A supercritical fluid dryer was used to perform supercritical drying of the wet gel. The wet gel was transferred into the supercritical drying chamber inside of a custom-built metal basket. Liquid CO_2 was introduced to exchange ethanol over 8 h and fresh CO_2 was introduced into the chamber every 15 min during the 8-h soaking period. The drying procedure was achieved at a temperature of 31 °C and a pressure of 1350 psi for 4 min, and gaseous CO_2 was bled at a rate of 100−150 psi/min to minimize pore collapse during evaporation of the CO_2 from the gel system.

X-ray Diffraction and Pair Distribution Function Analysis. An Inel CPS 120 (40 kV, 20 mA) powder diffraction equipped with graphite monochromatized Cu Kα (λ = 1.541 Å) radiation was used in asymmetric reflection mode to obtain diffraction intensity data from 10° to 100° in 2θ. The finely ground powder samples of aerogel were placed on top of a microscope slide for PXRD measurement. Pair distribution functions (PDF) were obtained using a high-energy synchrotron beam source of 58 keV (λ = 0.2128 Å) with the sample packed in a 1 mm Kapton capillary tube in transmission geometry. A MAR3450 image plate detector was used for the acquisition of the diffraction data, and a NIST silicon standard was used to calibrate the detector-to-sample distance. The Fit 2D software was used for the reduction of the two-dimensional (2D) diffraction patterns to intensity vs 2θ profiles. PDFgetX2 software was used to obtain the total scattering structure function,[32]

$$S(Q) = \frac{I^{coh}(Q) - \sum C_i |f_i(Q)|^2}{|\Sigma C_i f_i(Q)|^2} + 1 \quad (1)$$

which takes into account of the measured scattering intensity (I^{coh}), the atomic concentration (C_i), and the X-ray atomic form factor (f_i). The function $F(Q)$ ($F(Q) = [S(Q) - 1]$) was Fourier-transformed to $G(r)$, which provides the probability of finding two atoms separated by a radial distance r:[33]

$$G(r) = \frac{2}{\pi} \int_{Q=0}^{Q_{max}} Q[S(Q) - 1] \sin(Qr)\, dQ \quad (2)$$

$G(r)$ was then used to evaluate the local structure of the chalcogenide framework, as described earlier.[19,20,27,33]

Nitrogen Adsorption Measurements. The surface area and pore size distribution of the synthesized aerogels were measured by nitrogen adsorption/desorption isotherms, using a Micromeritics ASAP 2020 system at 77 K. The sample was degassed at 348 K under vacuum for 8 h before analysis, to remove any adsorbed impurities. The surface area was measured using the Brunauer−Emmett−Teller (BET) model for relative pressures in the range of 0.05−0.30 and the distribution of pore dimensions was calculated using the Barrett−Joyner−Halenda (BJH) model.[34]

Thermogravimetric Analysis. Thermal stability of chalcogel samples were measured using a Shimadzu Model TGA-50 system with handmade platinum foil basket. The temperature range was 25−600 °C, and the heating rate was 10 °C/min. Thermal analysis was conducted under a nitrogen atmosphere with a flow rate of 40 mL/min.

Optical Property Measurements. The diffuse reflectance UV−vis spectrum was measured using a Shimadzu Model UV-3101PC double-beam, double monochromator system in the 200−2500-nm range, to obtain the energy bandgap of the aerogel samples. $BaSO_4$ powder was used as a 100% reflectance standard. Diffuse reflectance data were converted to absorption data using the Kubelka−Munk function: $\alpha/s = (1 - R)^2/(2R)$ (where R is the measured reflectance, α the absorption coefficient, and s the scattering coefficient).[35]

Electron Microscopy Imaging and Elemental Analysis. The aerogel microstructures were imaged by scanning electron microscopy (SEM), and the relative atomic composition of the chalcogels was determined using energy-dispersive spectroscopy (EDS). A Hitachi Model S-3400N-II system was used with acceleration voltages of 20.0 kV, an acquisition time of 100 s, and the ESED II detector for elemental analysis. The samples were ground and positioned on a carbon-taped metal stub for image capture and elemental analysis. Carbon and oxygen content from EDS data were excluded from the calculation of relative Zn:Sn:S composition ratio for accuracy. Transmission electron microscopy (TEM) was used to view higher-resolution images of the zinc chalcogels, using a Hitachi Model H-8100 TEM instrument with an accelerating voltage of 200 kV and a 50k−80k magnification for image capture.

A Bruker S4 Explorer system was used for X-ray fluorescence (XRF) to attain the elemental compositions of the zinc chalcogels. The XRF data provided result complementary to the EDS data. The chalcogel samples were ground and pelletized in Kapton film for measurement. Analysis of the lighter elements (C, H, N, O) was performed by Midwest Micro Lab, Inc., to determine the presence of residual organic solvent (formamide) and acac ligand within the chalcogel framework. CHN and oxygen analysis was performed via combustion of chalcogel samples at 990 and 1200 °C, respectively, and gravimetric determination of the thermochemical decomposition was performed.

Particle Size Measurements. Small-angle X-ray scattering (SAXS) analysis was performed in order to estimate the average particle size in the chalcogels. Elastic scattering of X-rays at small angles (0.1°−10°) was used to provide information about the particle size.

Assuming a spherical shape, the average particle size of chalcogel was calculated based on scattering intensity using the Guinier approximation.[36−39] The scattering intensity (I) can be expressed in relation to the scattering vector (q) and the radius of gyration (R_G), which is the mean square distance from the center of gravity of the outermost electron shell of the analyte.[40]

$$I(q) = I_0 \exp\left(-\frac{1}{3}q^2{R_G}^2\right) \quad (3)$$

When the natural logarithm (ln) is applied, the relationship between R_G, I, and q^2 can be expressed as

$$\ln(I) = \ln(I_0)\left(-\frac{1}{3}q^2{R_G}^2\right) \quad (4)$$

Thus, when the natural logarithm of the scattering intensity I is plotted over the q^2 parameter, the slope of the fitting should be proportional to R_G. R_G, then, can be converted to an average particle diameter, using the following relationship to find the particle size:

$$D = 2\sqrt{{R_G}^2\left(\frac{5}{3}\right)} \quad (5)$$

Finely ground aerogel samples were held in a custom-built cell composed of a Kapton window (ca. 4 mm width) and zirconium foil (40 μm thick) for the measurement. A Bruker Hi-star 2-D wire detector with Cu rotating anode at 40 kV and 13 mA operating condition ($0.04\ Å^{-1} < q < 0.6\ Å^{-1}$) was used for the SAXS measurements. The sample-to-detector distance was measured using a Ag-behenate standard (d_{001} = 58.38 Å). 2D diffraction images were integrated into a one-dimensional (1D) diffraction pattern, as a function of q and the scattering intensity I with the FIT2D program.[41] The sample exposure time to the X-ray was 2 h for each sample.

Density Measurements. The skeletal density of the chalcogel samples was measured using a Micromeritics Model AccuPyc1340 system. A calibration standard of 0.718 cm^3 was used prior to the volume measurement. The density was calculated from the weight of the sample divided by the measured volume.

Heavy-Metal Removal Experiments. Aqueous solutions of Hg^{2+}, Cd^{2+}, Pb^{2+}, Fe^{2+}, and Zn^{2+} (100 mg/L) were prepared by the addition of $HgCl_2$, $Cd(CH_3COO)_2\cdot 2H_2O$, $Pb(CH_3COO)_2\cdot 3H_2O$, $FeCl_2$, $Cu(CH_3COO)_2\cdot H_2O$, and $Zn(NO_3)_2\cdot 6H_2O$ to 100 mL of H_2O. An amount of 10 mg of the $Zn^{2+}/[SnS_4]^{4-}$ chalcogel was suspended in 100 mL of each stock solution and stirred for 24 h. The resulting supernatant solutions were separated from the solids by two 30-min centrifugations. The supernatant solutions were analyzed using inductively coupled plasma−atomic emission spectroscopy (ICP-AES) to measure the heavy-metal removal capacity of the chalcogels. The target metal ion (Hg^{2+}, Cd^{2+}, Pb^{2+}, Zn^{2+}) concentrations were measured before and after treatment with the zinc chalcogels. A 1000 mg/L commercial solution (Aldrich or GFS Chemicals) of the respective ions was diluted with ultrapure water to produce solutions ranging from 1 mg/L to 20 mg/L for calibration. The supernatant sample solutions were also diluted to fit into the calibrated range. The efficiency of heavy-metal-ion remediation was expressed by the absorption capacity of chalcogel (q_e, from eq 6),[42] and the distribution coefficient (K_d, from eq 7):[43]

$$q_e = \frac{(C_0 - C_f)v}{m} \quad (6)$$

$$K_d = \frac{v[(C_0 - C_f)/C_f]}{m} \quad (7)$$

where V is the total volume of solution (given in liters); C_0 and C_f are, respectively, the initial and final equilibrium concentration of the metal ion solution (each given in units of mg/L); and m is the total amount chalcogel (absorbent) used in the solution (given in grams). The final units of adsorption capacity for chalcogel—mg (metal)/g (chalcogel)—was converted to mmol(metal)/g(chalcogel), so that the values could be compared with those of other materials.

Organic Molecule Absorption and Desorption. Fourteen milligrams (14 mg, 0.025 mmol) of $Zn^{2+}/[Sn_2S_6]^{4-}$chalcogel (ZTS-cg2) was suspended in 5 mL of a 1×10^{-3} M chloroform solution containing 1 mmol of either tetracyanoethylene (TCNE, 12.8 mg), tetrathialfulvalene (TTF, 20.4 mg), or anthracene (17.8 mg). The zinc chalcogels were soaked into the solutions for 48 h, filtered, and washed with anhydrous chloroform. The resulting chalcogel samples were dried in vacuum oven for 24 h and finely ground to a powder for UV−vis spectroscopy and infrared measurements. FT-IR spectroscopy was performed on a Nicolet 6700 FT-IR spectrometer in the mid (500−4000 cm^{-1}) IR region with 2 cm^{-1} resolution to confirm incorporation of organic molecules into chalcogels.

To calculate the amount of organic compound absorbed, the UV−vis optical absorbance of the TCNE/chloroform solution before and after treatment was monitored using a Perkin−Elmer LAMBDA 1050 spectrophotometer equipped with a double monochromator. The UV−vis absorption spectrum was measured in the 200−800 nm region, and the absorbance intensity (A) of a TCNE/chloroform solution with known concentration (1×10^{-3} M) was used to determine the molar absorption coefficient (ε) of TCNE in chloroform. This absorption coefficient was used to calculate the remaining concentration of TCNE solution and quantify the amount absorbed by the chalcogel (Beer−Lambert's law). The experimental absorption coefficient of TCNE in chloroform solution was $2 \times 10^4\ M^{-1}$ at 281 nm, which is similar to the average absorption coefficient of TCNE in various solvents ($15849\ M^{-1}$).[44]

RESULTS AND DISCUSSION

Metathesis Reactions and Chalcogel Formation. The metathesis reactions that give rise to the gelled chalcogenide networks are sensitive to the solution conditions, such as temperature, concentration, counterions, basicity, and solvent. Zinc coordination complexes with the bidentate ligand acetylacetonate (*acac*) were used as precursors to obtain slower reactions with anionic thiostannate clusters and prevent precipitation. Other zinc precursor salts with weakly bound monodentate ligands, such as acetate and nitrate, resulted in precipitation. The reaction temperatures also affect the reaction rate and polymerization processes. For example, at room temperature, more than one month of gelation time was required to observe rigid gels that were strong enough to withstand solvent exchange and critical point drying. When the temperature was adjusted to 60 °C, the polymerization and gelation processes were completed within 5 d. Metathesis reactions occurring at temperatures of >60 °C yielded precipitation or shrinkage of the gel volume, leading to smaller pore volumes and lower internal surface areas of the aerogels. Under the proper conditions, the polymerization process eventually led to rigid gels within 7−10 d: $Zn^{2+}/[SnS_4]^{4-}$ (eq 8) formed a cream-colored gel within 7 d, $Zn^{2+}/[Sn_2S_6]^{4-}$ (eq 9) formed a light yellow gel within 7 d, and $Zn^{2+}/[Sn_4S_{10}]^{4-}$ (eq 10) formed a light gray gel within 10 d.

$$2Zn^{2+} + [SnS_4]^{4-} \rightarrow Zn_2SnS_4\,(ZTS\text{-}cg1) \quad (8)$$

$$2Zn^{2+} + [Sn_2S_6]^{4-} \rightarrow Zn_2Sn_2S_6\,(ZTS\text{-}cg2) \quad (9)$$

$$2Zn^{2+} + [Sn_4S_{10}]^{4-} \rightarrow Zn_2Sn_4S_{10}\,(ZTS\text{-}cg3) \quad (10)$$

dx.doi.org/10.1021/cm2003462 |Chem. Mater. 2011, 23, 2447–2456

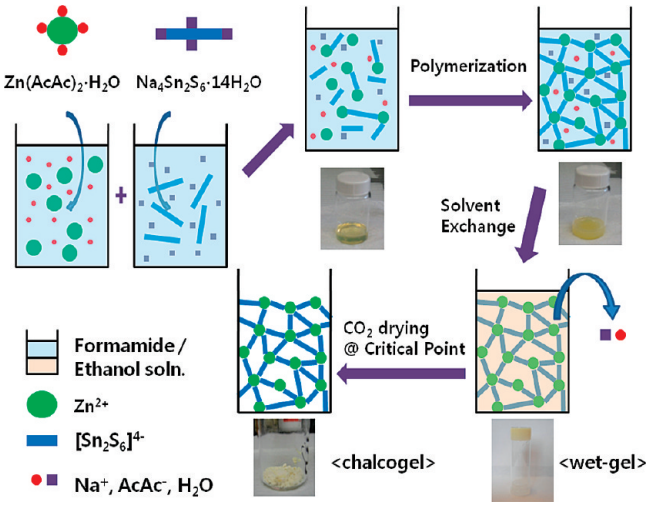

Figure 1. Schematic representation of the formation of $Zn^{2+}/[Sn_2S_6]^{4-}$ (ZTS-cg2) chalcogel via the metathesis route.

A schematic representation of the metathesis chalcogel reaction for the $Zn^{2+}/[Sn_2S_6]^{4-}$ system is summarized in Figure 1.

An optimized Zn^{2+}:$[Sn_xS_{2x+2}]^{4-}$:formamide molar ratio of 2:1:500 was used for all three Zn/Sn/S chalcogel syntheses. Higher concentrations of precursors (Zn^{2+}:$[Sn_xS_{2x+2}]^{4-}$:$HCONH_2$ = 2:1:200) tended to increase the chances of precipitation upon heat treatment, while lower concentrations (Zn^{2+}:$[Sn_xS_{2x+2}]^{4-}$:$HCONH_2$ = 2:1:1000) increased the gelation time and reduced the mechanical strength of the wet gels. Given the proper reaction temperature and concentration, the metal-chalcogenide solutions transformed to a thick and viscous sol state, where the chalcogenide clusters coordinate to the linking metal ions (Zn^{2+}) to form polymeric networks.

The metathesis reaction containing the 2:1 ratio of zinc linker and thiostannate clusters (ZTS-cg1, ZTS-cg2, and ZTS-cg3) all showed elemental compositions close to the stoichiometric ratios: $Zn_{1.6}SnS_{3.8}$, $Zn_{2.1}Sn_{2.0}S_{5.9}$, and $Zn_{2.6}Sn_4S_{10.1}$ from EDS analysis, and $Zn_{1.9}Sn_1S_{3.8}$, $Zn_{2.0}Sn_{2.0}S_{6.0}$, and $Zn_{2.2}Sn_{3.9}S_{9.5}$ from XRF measurement. This indicates that the coordination between the Zn^{2+} linker ions and $[Sn_xS_{2x+2}]^{4-}$ clusters forms a charge-balanced gel network.

The as-synthesized wet gels contain both formamide and byproducts within the inorganic framework; therefore, an ethanol solvent exchange is essential to remove them. C, H, N, and O analysis after washing showed the presence of organic species in the framework, where ZTS-cg2 and ZTS-cg3 have CHNO percentages of 5.38%, 1.37%, 2.18%, 5.52% and 8.06%, 1.96%, 2.21%, 6.41%, respectively. This indicates that some formamide and acetylacetonate ligand remains in the framework and are likely bound to Zn^{2+} ions.

Drying of the gels under ambient conditions yielded xerogels with significant volume reduction and very small surface areas (S_{BET} < 5 m^2/g), indicating the destruction of porosity during the evaporation of solvent. In order to preserve the pore space, the gels were dried with liquid CO_2 under supercritical conditions (300 K, 1070 psi) with a soaking period of longer than 8 h in CO_2 for maximized removal of solvent from the wet gel. The supercritical drying resulted in light gray (ZTS-cg1), light yellow (ZTS-cg2), and light salmon-colored (ZTS-cg3) granular aerogels.

PXRD, PDF, and SAXS Analysis. PXRD and PDF measurements were performed to investigate the long-range as well as the local structure of the chalcogel networks.[33] In the PXRD patterns of all zinc chalcogels, broad peaks were observed (Figure 2A), which indicates the lack of long-range order within the chalcogel structure. This is similar to previously reported chalcogels.[19,27] However, we observed that the Zn-chalcogel sample, when exposed to an X-ray beam for more than 8 h, began to show a more-distinct nanocrystalline ZnS phase (see Figure S 1 in the Supporting Information). This is the first example of X-ray sensitivity that has been observed in the chalcogel family.

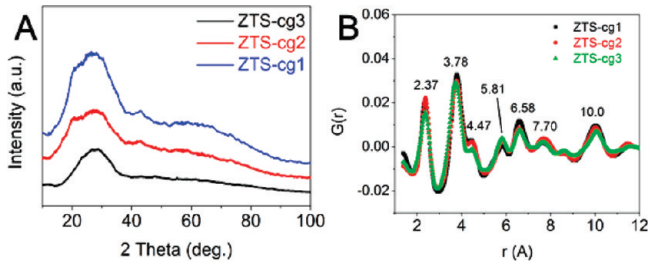

Figure 2. (A) Powder X-ray diffraction (XRD) patterns using a Cu Kα (λ = 1.541 Å) beam source on zinc chalcogels, showing broad diffraction peaks, which are indicative of an absence of an extended lattice structure for all three chalcogel samples. (B) Pair distribution function based on high-resolution XRD (58 keV, λ = 0.213 Å) of zinc chalcogel samples, showing various correlation vectors corresponding to the Zn−S, Sn−S nearest-neighbor and Zn···Sn and S···S next-nearest-neighbor distances.

PDF analysis of the total X-ray scattering pattern can provide useful information of the local structure and building blocks (molecular fragments) such as the ZTS-cg materials. However, the relative sensitivity of the sample to the high-intensity X-ray beam made it difficult to interpret the PDF data. The PXRD patterns of samples exposed to the X-ray beam for several hours using a Cu Kα source or for 90 s to a high-energy synchrotron X-ray beam (58 keV/λ = 0.2128 Å) appear to develop nanocrystalline ZnS within the amorphous network (see Figure 2B). Because the Zn−S, S−S, Zn−Zn distances in the ZnS phase closely matches with the thiostannate interatomic cluster distance of Sn−S and S−S, it is difficult to determine the source of the major vectors at 2.4, 3.8, 4.5, 5.8, 10.0 Å. However, these relative atomic vectors are very similar to meso-structured zinc tin sulfide materials, e.g., $(CP)_xZn_y$−Sn_2S_6 (where "(CP)" represents cetylpyridinium);[45] here, the cetylpyridinium acts as a structure-directing agent. Since ZTS-cg1 ($Zn^{2+}/[SnS_4]^{4-}$) and ZTS-cg2 ($Zn^{2+}/[Sn_2S_6]^{4-}$) have very similar PDF patterns, they likely have similar local structures, which are defined mainly by tetrahedral ZnS_4 and SnS_4 units.

Small-angle X-ray scattering (SAXS) is a powerful technique for probing materials with void space and nanosized features, and it can provide useful information about the particle size in the chalcogels. SAXS patterns are only observable when there is a difference in electron density within the structure.[46] For the ZTS-cg series, the scattering occurs at 0.063−0.065 nm^{-1}, and the average distance between particles (d = 2/q) is 96 nm. This seemingly large distance between particles accounts for the random aggregation of primary particles during the metathesis reaction and is associated with the large pores present in the ZTS-cg chalcogels. Based on the scattering intensity obtained from SAXS, the radius of gyration (R_g) was calculated for ZTS-cg1 (1.70 nm), ZTS-cg2 (2.01 nm), and ZTS-cg3 (1.92 nm), which reflects the spacial measure of a particle. Using Guinier's

dx.doi.org/10.1021/cm2003462 |Chem. Mater. 2011, 23, 2447–2456

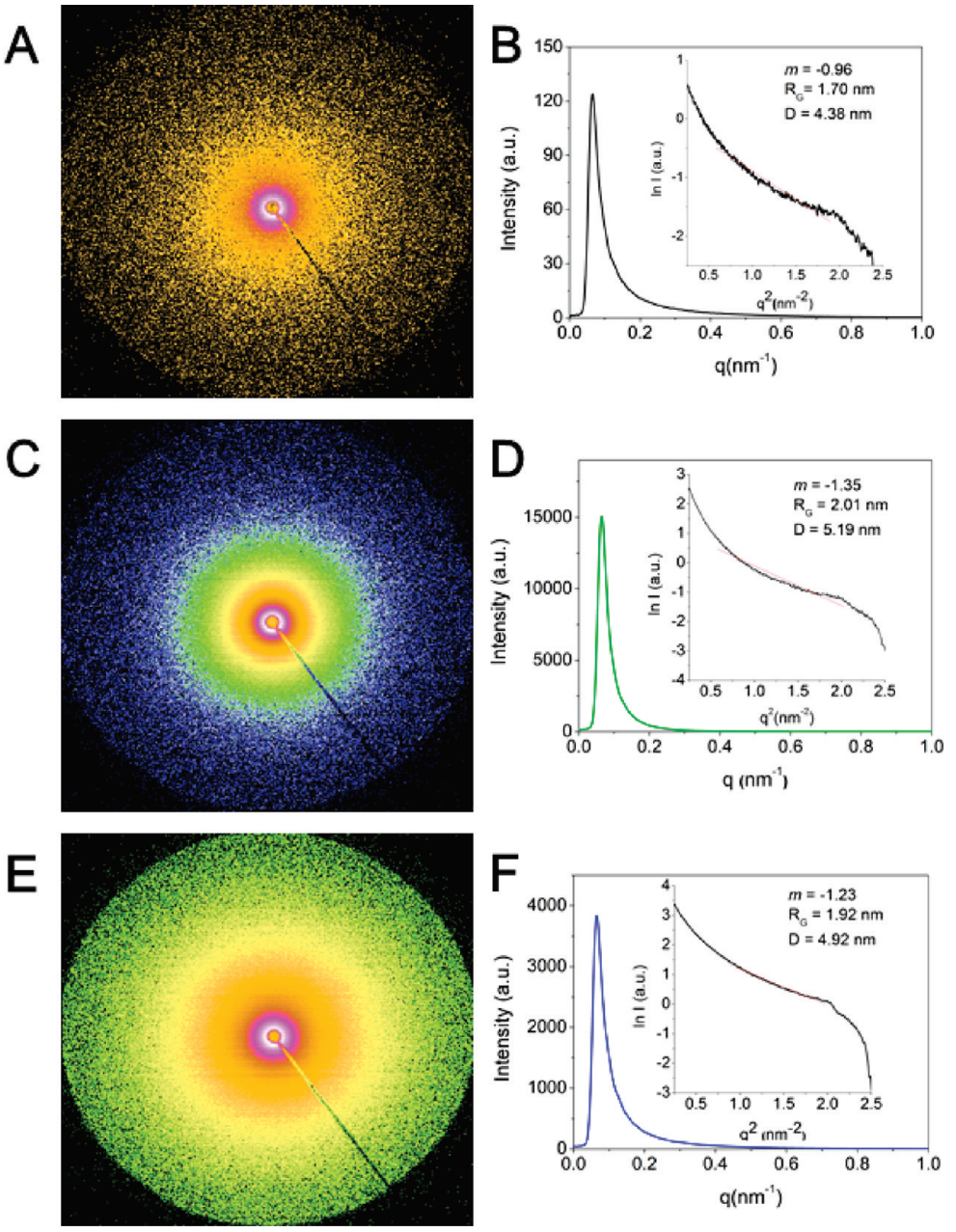

Figure 3. Two-dimensional (2D) scattering patterns of the ZTS-cg chalcogels ((A) ZTS-cg1, (C) ZTS-cg2, and (E) ZTS-cg3), as well as diffraction intensity plots and Guinier approximations of the average particle size based on fitted plots of $\ln(I)$ vs q^2 (inset plot) for the ZTS-cg chalcogels ((B) ZTS-cg1, (D) ZTS-cg2, and (F) ZTS-cg3). The diffuse scattering rings and small average particle size of the material confirms the amorphous structure of chalcogels, which was indicated by the PXRD patterns of these samples. The slope (m) of the linearly fitted plot of $\ln(I)$ vs q^2 is used to calculate the radius of gyration (R_G) and the average particle diameter (D).

approximation[47,48] and calculated R_g values, the average particle size of the chalcogel samples was estimated to be 4.4 ± 0.5 nm for ZTS-cg1, 5.2 ± 0.6 nm for ZTS-cg2, and 5.0 ± 0.5 nm for ZTS-cg3 (see Figure 3). By comparison, the particle size (D) and the average pore diameter (d) of $[MoS_4]^{4-}$-based chalcogels[27] are 5.2−23.2 nm and 24.6−45.8 nm, respectively.

Transmission and Scanning Electron Microscopy Analysis. Transmission electron microscopy (TEM) images of the ZTS chalcogels show amorphous aggregations of randomly shaped nanoparticles forming random porous networks with pore diameters of 5−100 nm (see Figures 4A−C). Darker areas indicate multilayer stacks of nanoparticles. The pore spaces represent the presence of formamide and other counterions during the metathesis reaction before the solvent exchange process. The absence of structure-directing agents allows particle aggregation of the inorganic species around the solvent molecules, yielding a random network. Electron diffraction patterns of these gels show diffuse rings proving the amorphous nature of the network. SEM images showed overall aggregation of particle growth at the micrometer scale (Figure 4D). The morphology of the chalcogels was consistent throughout the series, regardless of the size of the thiostannate clusters used to construct them.

Measurement of Optical and Chemical Properties. UV−vis diffuse reflectance spectroscopy shows bandgap energies at 2.89 eV

dx.doi.org/10.1021/cm2003462 |*Chem. Mater.* 2011, 23, 2447–2456

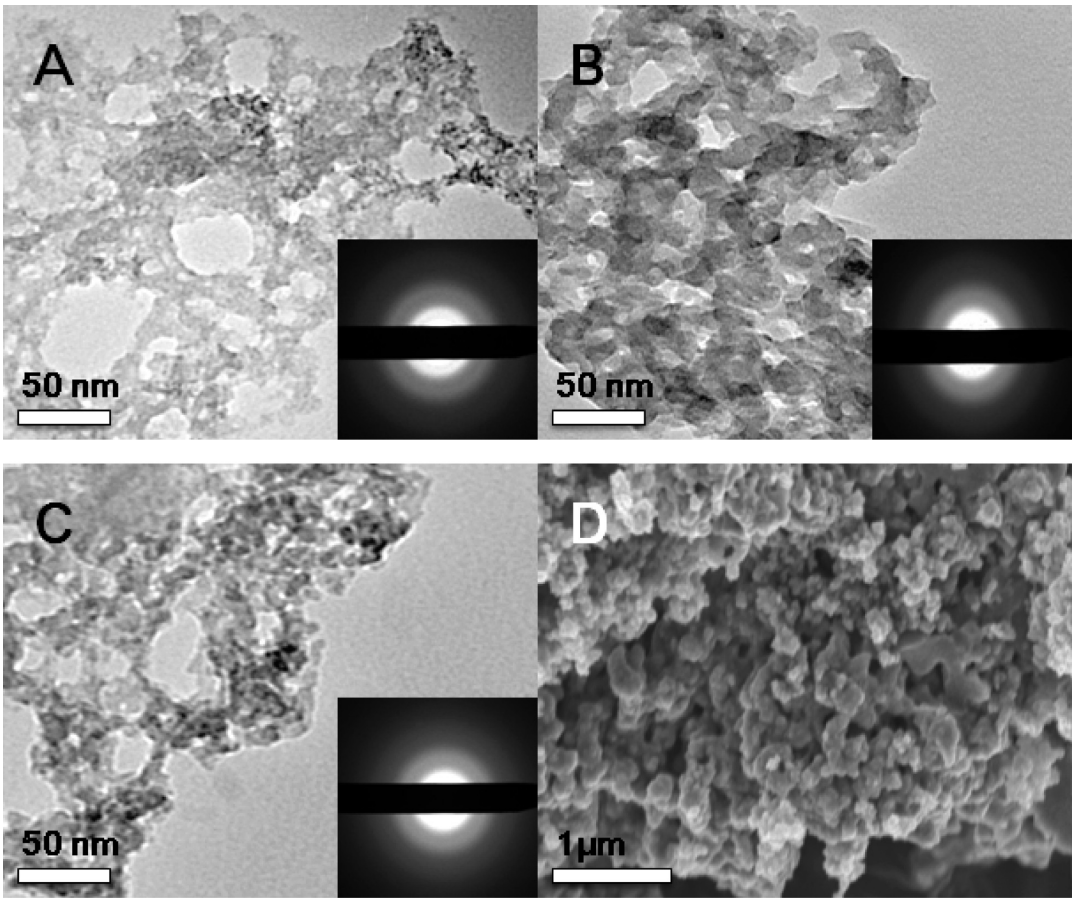

Figure 4. (A, B, C) TEM images of aerogels, showing the amorphous porous structure of the ZTS-cg chalcogels ((A) ZTS-cg1, (B) ZTS-cg2, and (C) ZTS-cg3). All of the samples exhibit diffuse diffraction rings, confirming the absence of a crystalline structure within the aerogel network. (D) SEM image showing an aggregation of particles interconnected by various pore sizes.

(430 nm) for ZTS-cg1, 3.14 eV (395 nm) for ZTS-cg2, and 3.23 eV (384 nm) for ZTS-cg3. (See Figure S 2 in the Supporting Information.) The absence of an observable absorption edge at 3.6 eV indicates that the different ZTS-cg chalcogels contain very little ZnS (e.g., <2%−4%). The elemental and optical properties of the chalcogels are summarized in Table 1. The difference in bandgap energy between ZTS-cg1 ($Zn^{2+}/[SnS_4]^{4-}$, 2.9 eV) and Chalcogel-6 (Pt/SnS_4, 1.4 eV)[20] is consistent with the general trend where the bandgap energy increases as the mean atomic number of the constituent atoms becomes smaller.[49,50]

Nitrogen Adsorption and Surface Area. The new chalcogel series described here features very high internal surface areas, large pore volumes, and a broad distribution of pore sizes. (See Table 1.) All three zinc chalcogels showed very similar nitrogen adsorption isotherm patterns: that is, minor adsorption at very low pressures ($P/P_0 < 0.05$), and major adsorption at higher pressures ($0.7 < P/P_0 < 1.0$), with a small hysteresis loop (see Figure 5). Both micropores ($d < 2$ nm) and slits between particles are expected to contribute to minor adsorption at lower pressures, whereas mesopores ($2 < d < 50$ nm) and macropores ($d > 50$ nm) play an active role in major adsorption at higher pressures. The presence of the small hysteresis loop indicates the slower desorption rate of nitrogen, compared to the adsorption rate, because of the percolation effect of random porous networks.[34]

The presence of pores within the materials is supported by the high BET surface areas (363−520 m^2/g) and large total pore volumes (1.2−1.6 cm^3/g) of the ZTS chalcogels. These surface areas correspond to 955−1965 m^2/g when normalized to the surface area of SiO_2 for the same number of atoms. BJH pore size distribution analysis shows a wide distribution of pore sizes, consistent with the absence of long-range order in the chalcogels. (See Figure 5D.) The average pore diameter of the chalcogels is within the range of 11.7−14.3 nm, as calculated from the surface area and total pore volume (assuming that the pore shape can be roughly approximated as being cylindrical. The skeletal densities of the zinc chalcogels are 3.30 ± 0.03 g/cm^3 for ZTS-cg1, 3.31 ± 0.02 g/cm^3 for ZTS-cg2, and 3.27 ± 0.03 g/cm^3 for ZTS-cg3, which explains the less-dense structure of the chalcogels, compared to the bulk ZnS (4.09 g/cm^3) and SnS_2 (4.50 g/cm^3).[51]

Thermal Analysis. The ZTS materials were studied using thermogravimetric analysis (TGA) to evaluate the thermal stability of the samples at elevated temperature under nitrogen. All $Zn^{2+}[Sn_xS_{2x+2}]^{4-}$ (x = 1, 2, 4) aerogel samples were dried in nitrogen at 100 °C to remove any adsorbed molecules before the measurement. Based on elemental analysis of the as-synthesized and dried samples, no degradation of the inorganic framework occurred during the drying process. No samples showed any weight loss until 180 °C, and then a gradual weight loss was observed as the temperature increased from 180 °C to 600 °C. At 600 °C, the samples lose 26%−30% of their weight (see Figure 6A), because of the loss of sulfur from the chalcogel framework, as confirmed by EDS analysis. (See Figure S 3 in the Supporting Information.)

Table 1. Elemental Composition, Optical Bandgap Energy, Pore Network Properties, and Density of Zn Chalcogels (ZTS-cg)

aerogel	ZTS-cg1	ZTS-cg2	ZTS-cg3
rel. atomic ratio (EDS)	$Zn_{1.6}SnS_{3.8}$	$Zn_{2.1}Sn_{2.0}S_{5.9}$	$Zn_{2.1}Sn_4S_{10.1}$
rel. atomic ratio (XRF)	$Zn_{1.9}SnS_{3.8}$	$Zn_{2.0}Sn_{2.0}S_{6.0}$	$Zn_{2.2}Sn_{3.9}S_{9.5}$
bandgap energy (eV)	2.9−3.0	3.0−3.1	3.2−3.3
surface area $_{BET}$ (m^2/g)	503−520	413−415	363−393
S_{BET} SiO_2 equiv. (m^2/g)	955−995	1219−1221	1815−1965
tot. pore vol. (cm^3/g)	1.5−1.6	1.1−1.3	1.3−1.4
avg. pore diameter (nm)	12.2−12.4	11.6−11.8	14.2−14.4
skeletal density (g/cm^3)	3.30 ± 0.03	3.31 ± 0.02	3.27 ± 0.03

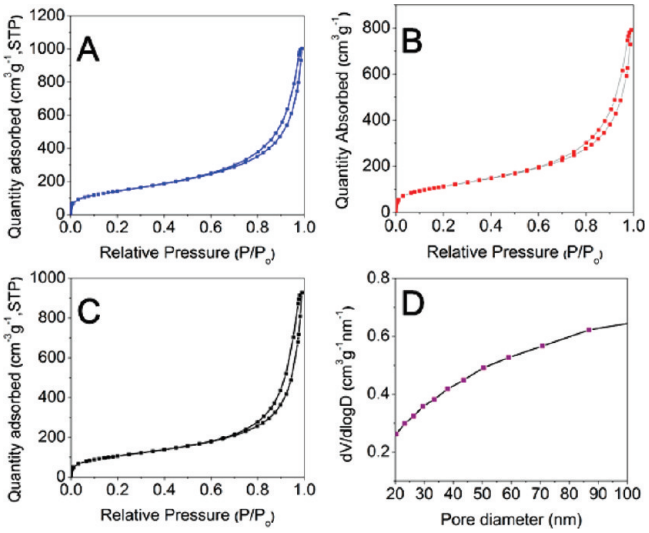

Figure 5. (A, B, C) Nitrogen adsorption and desorption isotherms of the ZTS-cg chalcogels ((A) ZTS-cg1, (B) ZTS-cg2, and (C) ZTS-cg3), showing type II isotherms with minor adsorption at low relative pressure and major adsorption at high relative pressure. (D) Consistent with the nature of aerogels, the BJH pore distribution of ZTS-cg1 (Zn^{2+}/$[SnS_4]^{4-}$) shows no specific distribution of pore size in the meso-macro pore size region (20−100 nm).

Comparison to the as-synthesized ZTS-cg2 sample shows that the ZnS phase becomes more distinct at 200 °C, but the overall amorphous structure remains. The amorphous chalcogel network appears to persist up to 400 °C, but crystalline SnO_2 and ZnO begin to appear, along with ZnS. As the temperature reaches 600 °C, the aerogel structures are completely destroyed and decompose to ZnO (space group $P6_3mc$), ZnS (space group $P6_3mc$), and SnO_2 (space group $P4_2/mnm$). (See Figure 6B.) The bound acetylacetonate ligand within the inorganic framework is believed to be a source of oxide, even in a flowing nitrogen or argon environment at higher temperature.

Experiments Involving the Removal of Heavy-Metal Ions. The wide sulfidic surfaces of the $Zn^{2+}/[Sn_xS_{2x+2}]^{4-}$ (ZTS-cg) chalcogels make them ideal candidates for studying the selective removal of soft heavy-metal ions from aqueous solution (see Table 2). During the suspension of the ZTS-cg chalcogel in the metal-ion solution, the sulfur sites act as soft Lewis bases and attract heavy transition-metal ions, which act as soft Lewis acids. As a result, heavy-metal ions such as Hg^{2+} replace the zinc from

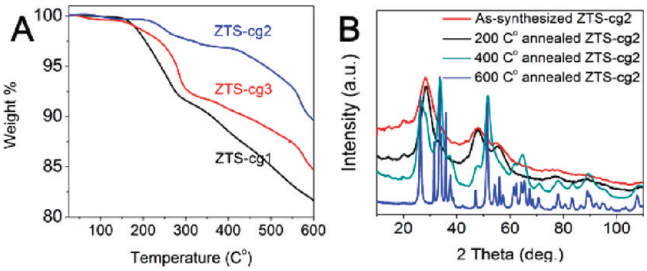

Figure 6. (A) Thermogravimetric analysis (TGA) of Zn chalcogels with a heating rate of 5 °C/min under nitrogen, showing a gradual weight loss above 200 °C. (B) PXRD pattern of a TGA sample treated at different temperatures (200−600 °C), indicating the progressive destruction of the amorphous aerogel structure and oxidization, resulting in a mixture of ZnO, SnO_2, and ZnS.

the ZTS-cg network through an ion-exchange reaction (eq 11):

$$2Hg^{2+} + Zn_2Sn_2S_6 \rightarrow Hg_2Sn_2S_6 + 2Zn^{2+} \qquad (11)$$

The strong affinity of Hg^{2+} toward the sulfidic surfaces of the aerogels is emblematic of the hard soft acid−base theory proposed by Pearson.[52] The ZTS-cg1 system showed high distribution coefficient (K_d) values: 1.62×10^6 mL/g for Hg^{2+}, 1.02×10^5 mL/g for Pb^{2+}, and 3.13×10^4 mL/g for Cd^{2+} solution. Chalcogels composed of larger clusters such as $[Sn_2S_6]^{4-}$ and $[Sn_4S_{10}]^{4-}$ exhibited greater affinities for heavy-metal ions. For instance, ZTS-cg2 and ZTS-cg3 exhibited K_d values of 2.80×10^7 mL/g and 1.10×10^8 mL/g, respectively, toward Hg^{2+} solution.

The ZTS-cg3 sample was used to test ion selectivity in a solution containing Hg^{2+}, Cd^{2+}, Pb^{2+}, Zn^{2+}, and Fe^{2+} ions. The chalcogel showed very high efficiency in the removal of Hg^{2+} (99.9% removal, 1.12×10^8 mL/g), Cd^{2+} (99.8% removal, 4.81×10^6 mL/g), and Pb^{2+} (98.8% removal, 8.46×10^5 mL/g), Zn^{2+} (79.8% removal, 3.98×10^4 mL/g), whereas lighter and harder ions such as Fe^{2+} (6.7% removal, 7.95×10^3 mL/g) showed lower affinity toward the chalcogels. The Hg^{2+} removal rate of ZTS-cg3 is comparable to materials known for their high mercury-removal efficiency, such as Chalcogel-1 (Pt/Ge_4S_{10}, $0.92-1.61 \times 10^7$ mL/g),[20] and LHMS-1 (layered hydrogen metal sulfide, $H_{2x}Mn_xSn_{3-x}S_6$ [$x = 0.5-0.95$], $3.2 \times 10^6-1.09 \times 10^7$ mL/g).[53]

The ZTS-cg chalcogel series shows higher adsorption capacity for Hg^{2+} (1.40−1.69 mmol/g) than the functionalized mesoporous silicas, such as MBT-SBA-15 (0.10−0.24 mmol/g), MBT-MCM-41 (0.13−0.21 mmol/g) (MBT = 2-mercaptobenzothiazol),[54] and SH-ePMO (0.32 mmol/g).[55] This high adsorption capacity of ZTS-cg chalcogels also exists for other heavy metals, such as Pb^{2+} (1.53−1.63 mmol/g), Cd^{2+} (1.94−2.85), and Cu^{2+} (3.95 mmol/g), in contrast to the lower adsorption capacity of NH_2-MCM-41[56] (functionalized amino silica) for Pb^{2+} (0.28 mmol/g) and Cd^{2+} (0.16−0.71 mmol/g), and SH-SBA-16[42] (thiol-functionalized silica) for Cu^{2+} (0.16−0.55 mmol/g). These results show that the ZTS-cg can be used as a heavy-metal remediation medium for aqueous solutions without any specific functionalization.

Absorption of Organic Molecules. The accessible open space and wide surface areas of ZTS-cg chalcogels allows surface interaction and functionalization with guest molecules. Unlike the vast majority of porous materials that feature oxidic or carbon-based surfaces available for interaction with guest molecules, the

dx.doi.org/10.1021/cm2003462 |Chem. Mater. 2011, 23, 2447–2456

Table 2. Adsorption of Divalent Metal Ions by Zn−Sn_xS_{2x+2} Aerogels and Selected Functionalized Mesoporous Silicas

		Concentration of Aqueous Metal Ions in Solution (mg/L)				
M^{2+}	aerogel	initial, C_i	equilibrium, C_f (mg/L)	M^{2+} removal (%)	q_e[a] (mmol/g)	K_d[b] (mL/g)
Hg	ZTS-cg1	93	0.57	99.4	1.40	1.62×10^6
	ZTS-cg2	112	0.04	99.2	1.69	2.80×10^7
	ZTS-cg3	112	0.01	99.9	1.69	1.12×10^8
	MBT-SBA-15[c]				0.10−0.24	
	MBT-MCM-41[d]				0.13−0.21	
	SH-ePMO[e]				0.32	
Pb	ZTS-cg1	115	10.3	91.0	1.53	1.02×10^5
	ZTS-cg3	113	1.32	98.8	1.63	8.46×10^5
	NH_2-MCM-41[f]				0.28	
Cd	ZTS-cg1	95	23	75.8	1.94	3.13×10^4
	ZTS-cg3	106	0.22	99.8	2.85	4.81×10^6
	NH_2-MCM-41[f]				0.16−0.71	
Cu	ZTS-cg3	94	8.52	91.0	3.95	1.00×10^5
	SH-SBA-16[g]				0.16−0.55	
Zn	ZTS-cg3	112	22.5	79.8	4.15	3.98×10^5
Fe	ZTS-cg3	94.2	88.0	6.56	0.34	7.05×10^3

[a] The metal ion absorption capacity of the chalcogel. [b] An aerogel contents volume-to-mass ratio of 10 000 mL/g was used in solution. [c] 2-mercaptobenzothiazol(MBT) functionalized SBA-15 (mesoporous silica). [d] 2-mercaptobenzothiazol(MBT) functionalized MCM-41 (mesoporous silica). [e] Thiol-functionalized (bridged with ethane) periodic mesoporous organosilica. [f] Amino-functionalized MCM-41. [g] Thiol-functionalized SBA-16.

Table 3. Summary of Infrared Spectra of TCNE, ZTS-cg2, and TCNE/ZTS-cg2,[a] Recorded as KBr or CsI Pellets

	ν_{O-H}	$\nu_{C\equiv N}$[b]	$\nu_{C=O}$[c]	ν_{C-C-C}[c]
TCNE		2260(s); 2227(s); 2214(s)		
ZTS-cg2	3420−2730(s)		1677(s); 1596(m)	1246(m)
TCNE/ZTS-cg2	3300−3030(s)	2246(s); 2225(s); 2210(s)	1650(s); 1600(s)	1250(m)

[a] The ZTS-cg2 sample was treated with a 1×10^{-3} M TCNE/$CHCl_3$ solution for 24 h, filtered, and dried under nitrogen. [b] Data taken from ref 62. [c] Data taken from ref 63.

chalcogels have surfaces covered with softer and more-polarizable sulfide ions. Therefore, they present a new opportunity to study interactions with a variety of molecules. In this context, we tested molecules with electron-acceptor and electron-donor properties. The ZTS-cg2 chalcogel selectively absorbs TCNE, which is an electron-accepting molecule, from chloroform solution; no interaction was observed with TTF, which is a strong electron-donating molecule, or with anthracene, which is a more-inert molecule with low electron transfer ability.[57−61]

The absorption of TCNE in ZTS-cg2 was confirmed with infrared spectroscopy. (See Table 3.) The infrared absorption peaks at 2260(s), 2227(m), and 2214(w) cm^{-1} are the characteristic vibration modes of TCNE that arise from the nitrile (C≡N) groups. The as-synthesized ZTS-cg2 samples do not show absorption peaks in this region (see Figure 7A). ZTS-cg2 samples containing TCNE show vibration peaks at 2246(m), 2225(s), and 2210(s) cm^{-1}, which are slightly shifted to lower frequencies that match the bands of typical TCNE-electron donor group complexes.[62] We expect the presence of the C≡N group with its low-lying π^* orbitals to draw electron density from the chalcogel network. Other IR bands of the TCNE/ZTS-cg2 sample in the 3300−3000 cm^{-1} (ν_{O-H}), 1650−1600 cm^{-1} ($\nu_{C=O}$), and 1250 cm^{-1} (ν_{C-C-C}) regions most likely correspond to the residual Zn-bound acetylacetonate ligand in the framework.[63]

TCNE absorption by the ZTS-cg2 causes a red shift in its bandgap energy, as revealed by UV−vis spectroscopy. The higher the TCNE absorption, the higher the degree of bandgap shift (see Figure 7B). Namely, the bandgap of ZTS-cg2 at 3.1 eV moves to the 2.6−2.8 eV region upon adsorption of TCNE from a chloroform solution. This suggests that the incorporation of TCNE into the ZTS chalcogel network results in a donor−acceptor charge-transfer interaction where the chalcogel acts as an electron donor. The bandgap changes in the chalcogel upon TCNE absorption can be understood with an donor−acceptor interaction, where the valence band of the Zn−Sn−S chalcogel donates charge to the lowest unoccupied molecular orbital (LUMO) of TCNE. A similar phenomenon of bandgap reduction has been reported in other TCNE-incorporated materials.[39,64] In the absence of a detailed structure model for this system, however, it is difficult to explain the reduction in bandgap. The amount of TCNE absorbed by the chalcogel was calculated using the UV−vis absorbance intensity difference of a 1×10^{-2} M TCNE/$CHCl_3$ solution and supernatant TCNE/$CHCl_3$ solution after the addition of chalcogel. Based on the absorption coefficient, the amount of TCNE absorbed in ZTS-cg2 corresponds to 0.25 equiv per formula unit.

The TCNE molecules could be desorbed from the chalcogel network by washing with ethanol. Within 48 h, the dark brown aerogel transformed to a light brown color, and further ethanol

dx.doi.org/10.1021/cm2003462 |Chem. Mater. 2011, 23, 2447–2456

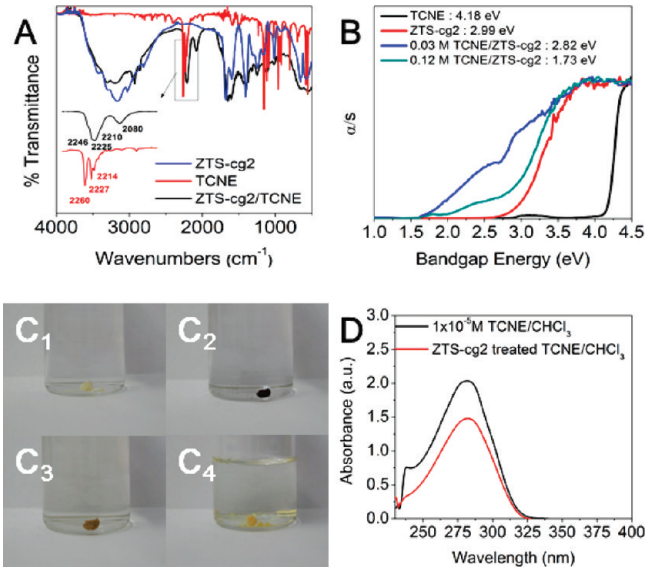

Figure 7. Mid-IR spectra of ZTS-cg2 treated with tetracyanoethylene (TCNE)/chloroform. The spectra show that ZTS chalcogels selectively absorb and interact with the TCNE. (A) Infrared spectra showing the C≡N vibration peaks shift to lower energy, confirming the charge-transfer interaction between chalcogel and TCNE. (B) UV−vis spectra of the as-synthesized ZTS and chalcogel samples treated with different TCNE concentrations of $CHCl_3$ solution; the effect of TCNE absorption is shown by the marked red shift of the bandgap energy. (C_1−C_4) Photographs showing the changes in as-synthesized ZTS-cg2 in TCNE/chloroform solution: (C_1) as-synthesized ZTS-cg2 in chloroform; (C_2) the sample turns dark brown upon absorbing TCNE from a 1×10^{-2} M TCNE/chloroform solution over 24 h; and then ethanol causes a desorption of TCNE with a progressive color change toward the original chalcogel color (yellow) ((C_3) within 24 h and (C_4) within 72 h). (D) The concentration of TCNE absorbed by ZTS-cg2 was calculated from the difference in absorbance intensity of TCNE/chloroform solution of solution UV−vis spectroscopy.

soaking for 24 h resulted in the original ZTS yellow color of the TCNE-free chalcogel (recall Figure 7). The supernatant ethanol solution showed a strong absorbance at 230 nm, confirming the presence of TCNE and demonstrating the reversibility of the adsorption/desorption process and the charge-transfer nature of the interaction. This result suggests that the chalcogels can discriminate among organic conjugated molecules on the basis of electronic structure and could be used as active materials for the selective absorption of a variety of electron-acceptor molecules.

CONCLUDING REMARKS

The reaction of $[Sn_xS_{2x+2}]^{4-}$ clusters with Zn^{2+} ions coordinated with acetylacetonate (*acac*) ligands produced in random networks that can form stable gels. Control of the metathesis conditions such as temperature, counterion, and time of polymerization greatly affects the ability to form gels and the properties of the resulting chalcogels. Metal precursors with bidentate ligands allow for a more-controlled metathesis process and provides labile self-assembly conditions that can lead to gelation. The wet gels can then sustain a supercritical drying process to yield high-surface-area aerogels. As previous chalcogels have demonstrated, the transition-metal linker greatly affects the optical and electronic properties. The zinc chalcogels feature highly selective surfaces that can remove soft heavy-metal ions (such as Hg^{2+}, Cd^{2+}, and Pb^{2+}) from aqueous media. In addition, the ZTS networks engage in reversible adsorption of electron-accepting molecules such as TCNE via charge transfer processes. The adsorption of organic acceptor molecules causes a reversible visible shift in the bandgap energy, permitting these materials to be tuned for desirable applications such as sensors, thin-film transistors, and other optical devices.

ASSOCIATED CONTENT

Supporting Information. This material is available free of charge via the Internet at http://pubs.acs.org.

AUTHOR INFORMATION

Corresponding Author
*E-mail: m-kanatzidis@northwestern.edu.

ACKNOWLEDGMENT

This research was supported in part by the Nanoscale Science and Engineering Initiative of the National Science Foundation (under NSF Award No. EEC 0647560) and in part by Office of Naval Research (No. N00014-10-1-0331). ICP−AES measurements were made at Analytical Service Laboratory (ASL) facilities, and SAXS, as well as XRF, data were collected from the J. B. Cohen X-ray Diffraction Facility at Northwestern University. ICP-MS analysis was performed at the Quantitative Bioelemental Imaging Center (QBIC). Solution UV−vis analysis was performed at the Keck Biophysics Facility, and electron microscopy imaging work (SEM, TEM) was performed at the EPIC facility of the NUANCE Center at Northwestern University. The NUANCE Center is supported by NSF-NSEC, NSF-MRSEC, the Keck Foundation, the State of Illinois, and Northwestern University. Work performed at Argonne National Laboratory and use of the Advanced Photon Source for PDF and PXRD were supported by the U.S. Department of Energy, Office of Science, Office of Basic Energy Sciences (under Contract No. DE-AC02-06CH11357).

REFERENCES

(1) Rolison, D. R. *Science* **2003**, *299* (5613), 1698–1701.
(2) Pajonk, G. M. *Appl. Catal.* **1991**, *72* (2), 217–266.
(3) Schneider, M.; Baiker, A. *Catal. Today* **1997**, *35* (3), 339–365.
(4) Husing, N.; Schubert, U.; Misof, K.; Fratzl, P. *Chem. Mater.* **1998**, *10* (10), 3024–3032.
(5) Ko, E. I. *Chem. Technol.* **1993**, *23* (4), 31–36.
(6) Sui, R. H.; Liu, S. Y.; Lajoie, G. A.; Charpentier, P. A. *J. Sep. Sci.* **2010**, *33* (11), 1604–1609.
(7) Delaizir, G.; Lucas, P.; Zhang, X. H.; Ma, H. L.; Bureau, B.; Lucas, J. *J. Am. Ceram. Soc.* **2007**, *90* (7), 2073–2077.
(8) Leventis, N.; Elder, I. A.; Rolison, D. R.; Anderson, M. L.; Merzbacher, C. I. *Chem. Mater.* **1999**, *11* (10), 2837–2845.
(9) Rolison, D. R.; Dunn, B. *J. Mater. Chem.* **2001**, *11* (4), 963–980.
(10) Husing, N.; Schubert, U. *Angew. Chem., Int. Ed.* **1998**, *37* (1−2), 23–45.
(11) Mills, A.; LeHunte, S. *J. Photochem. Photobiol. A—Chem.* **1997**, *108* (1), 1–35.
(12) Auborn, J. J.; Barberio, Y. L.; Hanson, K. J.; Schleich, D. M.; Martin, M. J. *J. Electrochem. Soc.* **1987**, *134* (3), 580–586.
(13) Lokhande, C. D.; Ennaoui, A.; Patil, P. S.; Giersig, M.; Diesner, K.; Muller, M.; Tributsch, H. *Thin Solid Films* **1999**, *340* (1−2), 18–23.
(14) Grasso, C.; Nanu, M.; Goossens, A.; Burgelman, M. *Thin Solid Films* **2005**, *480*, 87–91.

(15) Mohanan, J. L.; Arachchige, I. U.; Brock, S. L. *Science* **2005**, *307* (5708), 397–400.
(16) Husing, N. *Sol−Gel Methods Mater. Process.* **2008**, 91–104.
(17) Arachchige, I. U.; Brock, S. L. *Acc. Chem. Res.* **2007**, *40* (9), 801–809.
(18) Shriver, D. F.; Atkins, P. W.; Overton, T. L.; Rourke, J. P.; Weller, M. T.; Armstrong, F. A. *Shriver & Atkins Inorganic Chemistry*; W. H. Freeman and Company: New York, 2006.
(19) Bag, S.; Arachchige, I. U.; Kanatzidis, M. G. *J. Mater. Chem.* **2008**, *18* (31), 3628–3632.
(20) Bag, S.; Trikalitis, P. N.; Chupas, P. J.; Armatas, G. S.; Kanatzidis, M. G. *Science* **2007**, *317* (5837), 490–493.
(21) Allen, G. C.; Paul, M.; Dunleavy, M. *Adv. Mater.* **1992**, *4* (6), 424–427.
(22) Stanic, V.; Etsell, T. H.; Pierre, A. C.; Mikula, R. J. *Mater. Lett.* **1997**, *31* (1−2), 35–38.
(23) Stanic, V.; Pierre, A. C.; Etsell, T. H.; Mikula, R. J. *J. Non-Cryst. Solids* **1997**, *220* (1), 58–62.
(24) Stanic, V.; Pierre, A. C.; Etsell, T. H.; Mikula, R. J. *J. Phys. Chem. A* **2001**, *105* (25), 6136–6143.
(25) Kalebaila, K. K.; Georgiev, D. G.; Brock, S. L. *J. Non-Cryst. Solids* **2006**, *352* (3), 232–240.
(26) Arachchige, I. U.; Mohanan, J. L.; Brock, S. L. *Chem. Mater.* **2005**, *17* (26), 6644–6650.
(27) Bag, S.; Gaudette, A. F.; Bussell, M. E.; Kanatzidis, M. G. *Nature Chem.* **2009**, *1* (3), 217–224.
(28) Shafaei-Fallah, M.; He, J.; Rothenberger, A.; Kanatzidis, M. G. *J. Am. Chem. Soc.* **2011**, *133* (5), 1200–1202.
(29) Bag, S.; Kanatzidis, M. G. *J. Am. Chem. Soc.* **2010**, *132* (42), 14951–14959.
(30) Tsamourtzi, K.; Song, J. H.; Bakas, T.; Freeman, A. J.; Trikalitis, P. N.; Kanatzidis, M. G. *Inorg. Chem.* **2008**, *47* (24), 11920–11929.
(31) Tousimis Autosamdri-815B Series A was used as the supercritical fluid drying process. The wet gel was transferred into a supercritical drying chamber and fresh liquid CO_2 was introduced to exchange EtOH from wet gel into liquid CO_2. The steps of filling with fresh CO_2, washing with EtOH, and draining were repeated every 15 min for 7 h. Drying of the sample was achieved at elevated temperature and pressure (31 °C, 1350 ± 5% psi) for 4 min, and gaseous CO_2 was bled at 100−150 psi/min.
(32) Qiu, X.; Thompson, J. W.; Billinge, S. J. L. *J. Appl. Crystallogr.* **2004**, *37*, 678.
(33) Billinge, S. J. L.; Kanatzidis, M. G. *Chem. Commun.* **2004**, *7*, 749–760.
(34) Rouquerol, F.; Rouquerol, J.; Sing, K. *Adsorption by Powders and Porous Solids: Principles, Methodology, and Applications*; Academic Press: San Diego, CA, 1999.
(35) (a) Mccarthy, T. J.; Kanatzidis, M. G. *Chem. Mater.* **1993**, *5* (8), 1061–1063. (b) Liao, J. H.; Kanatzidis, M. G. *Chem. Mater.* **1993**, *5*, 1561–1569. (c) Chondroudis, K.; McCarthy, T. J.; Kanatzidis, M. G. *Inorg. Chem.* **1996**, *35*, 840–844. (d) Liao, J. H.; Varotsis, C.; Kanatzidis, M. G. *Inorg. Chem.* **1993**, *32*, 2453–2462.
(36) Kratky, O.; Stabinger, H. *Colloid Polym. Sci.* **1984**, *262* (5), 345–360.
(37) Armatas, G. S.; Kanatzidis, M. G. *Nano Lett.* **2010**, *10* (9), 3330–3336.
(38) (a) Armatas, G. S.; Kanatzidis, M. G. *Nature* **2006**, *441* (7097), 1122–1125. (b) Armatas, G. S.; Kanatzidis, M. G. *Science* **2006**, *313*, 817–820.
(39) Armatas, G. S.; Kanatzidis, M. G. *Adv. Mater.* **2008**, *20* (3), 546–550.
(40) Muller, J.; Lothman, P.; Meyer, D. C. *Cryst. Res. Technol.* **2005**, *40* (1−2), 177–181.
(41) Hammersley, F. A. P. *FIT2D*, 9.129; France, 1998.
(42) Xue, X. M.; Li, F. T. *Microporous Mesoporous Mater.* **2008**, *116* (1−3), 116–122.
(43) Manos, M. J.; Malliakas, C. D.; Kanatzidis, M. G. *Chem.—Eur. J.* **2007**, *13* (1), 51–58.
(44) Nyquist, R. A. *The Handbook of Infrared and Raman Spectra of Inorganic Compounds and Organic Salts*; Academic Press: San Diego, CA, 1997; Vol. 4.
(45) Rangan, K. K.; Trikalitis, P. N.; Canlas, C.; Bakas, T.; Weliky, D. P.; Kanatzidis, M. G. *Nano Lett.* **2002**, *2* (5), 513–517.
(46) Glatter, O.; Kratky, O. *Small Angle X-ray Scattering*; Academic Press: New York, 1982.
(47) Hight, R.; Higdon, W. T.; Schmidt, P. W. *J. Chem. Phys.* **1960**, *33* (6), 1656–1661.
(48) Schmidt, P. W. *Modern Aspects of Small-Angle Scattering*; Kluwer Academic Publishers: Dordrecht, The Netherlands, 1995.
(49) Nag, B. R. *Infrared Phys. Technol.* **1995**, *36* (5), 831–835.
(50) McKelvey, J. P. *Solid State and Semiconductor Physics*; Harper & Row: New York, 1966.
(51) Wells, A. F. *Structural Inorganic Chemistry*, 5th ed.; Clarendon Press/Oxford University Press: Oxford, Oxfordshire, New York, 1984.
(52) Pearson, R. G. *J. Am. Chem. Soc.* **1963**, *85* (22), 3533–3539.
(53) Manos, M. J.; Petkov, V. G.; Kanatzidis, M. G. *Adv. Funct. Mater.* **2009**, *19* (7), 1087–1092.
(54) Perez-Quintanilla, D.; del Hierro, I.; Fajardo, M.; Sierra, I. *J. Environ. Monit.* **2006**, *8* (1), 214–222.
(55) De Canck, E.; Lapeire, L.; De Clercq, J.; Verpoort, F.; Van Der Voort, P. *Langmuir* **2010**, *26* (12), 10076–10083.
(56) Heidari, A.; Younesi, H.; Mehraban, Z. *Chem. Eng. J.* **2009**, *153* (1−3), 70–79.
(57) Wegner, D.; Yamachika, R.; Wang, Y.; Brar, V. W.; Bartlett, B. M.; Long, J. R.; Crommie, M. F. *Nano Lett.* **2008**, *8* (1), 131–135.
(58) Murata, T.; Morita, Y.; Yakiyama, Y.; Fukui, K.; Yarnochi, H.; Saito, G.; Nakasuji, K. *J. Am. Chem. Soc.* **2007**, *129* (35), 10837–10846.
(59) Foster, R. *J. Phys. Chem.* **1980**, *84* (17), 2135–2141.
(60) Odom, S. A.; Caruso, M. M.; Finke, A. D.; Prokup, A. M.; Ritchey, J. A.; Leonard, J. H.; White, S. R.; Sottos, N. R.; Moore, J. S. *Adv. Funct. Mater.* **2010**, *20* (11), 1721–1727.
(61) Alves, H.; Molinari, A. S.; Xie, H. X.; Morpurgo, A. F. *Nat. Mater.* **2008**, *7* (7), 574–580.
(62) Miller, J. S. *Angew. Chem., Int. Ed.* **2006**, *45* (16), 2508–2525.
(63) Smith, B. *Infrared Spectral Interpretation: A Systematic Approach*; CRC Press: Boca Raton, FL, 1999.
(64) Pappenfus, T. M.; Hermanson, B. J.; Helland, T. J.; Lee, G. G. W.; Drew, S. M.; Mann, K. R.; McGee, K. A.; Rasmussen, S. C. *Org. Lett.* **2008**, *10* (8), 1553–1556.